JMEPEG (2005) 14:327-342
DOI: 10.1361/10599490523977

1059-9495/$19.00

Evaluation of Microstructure and Electrochemical Corrosion Behavior of Austenitic 316 Stainless Steel Weld Metals with Varying Chemical Compositions

M.G. Pujar, R.K. Dayal, S.N. Malhotra, and T.P.S. Gill

(Submitted August 6, 2004; in revised form March 21, 2005)

Austenitic stainless steel weld metals have, in general, inferior corrosion resistance compared with the base metals. This is due to the fact that the weld metal has an inhomogeneous and dendritic microstructure with microsegregation of major elements (i.e., Cr, Mo, and Ni) as well as minor elements (i.e., S and P) at the δ-γ interface boundaries. The nonuniform alloying element concentration around ferrite particles plays a major role in determining the electrochemical corrosion behavior of such weld metals. Although the presence of ferrite is considered to be detrimental as far as the localized corrosion is considered, its exact role in uniform corrosion is still not clear. The uniform corrosion behavior of an alloy is determined by the fundamental electrochemical parameters of the major alloying elements. In this study, an attempt has been made to correlate the microstructure and uniform corrosion behavior of type 316 stainless steel weld metals with varying concentrations of Cr and Mo, and different ferrite contents. From the empirical equations obtained during the analysis of the electrochemical corrosion data, an attempt has been made to understand the role of Cr, Mo, and ferrite in altering the electrochemical corrosion parameters of the weld metal. Based on the extensive microstructural characterization, a dissolution model for the weld metal in the moderately oxidizing medium has been proposed.

Keywords: austenitic stainless steel, delta-ferrite, electrochemical corrosion, welding

1. Introduction

It is well known that the cycle of rapid heating and cooling that occurs during welding affects the microstructure and surface composition of welds. Consequently, the corrosion resistance of autogenous welds and welds made of matching filler metals is inferior to that of the base metal. Among the various factors that affect corrosion behavior, the microsegregation of alloying elements is found to be a prominent one (Ref 1). Heat input and welding technique affect the solidification behavior of weld metals, thereby affecting its corrosion performance (Ref 2). The microsegregation of Cr and Mo during weld solidification and cooling in type 316 and type 316L weld metals have been extensively studied by a number of investigators (Ref 3-7). They concluded that the microsegregation of Cr and, particularly, Mo (Ref 4, 5) was found to be much higher at the δ-γ interphase boundaries. The segregated Mo was reported to be more detrimental to the uniform corrosion of high-alloyed austenitic stainless steels (Ref 8). The presence of 2 to 10% of the delta-ferrite is considered as a prerequisite to avoid solidification cracking during welding (Ref 9), but this ferrite was attacked in certain corrosive media leading to component failures (Ref 10, 11). It was also reported that the surface dendrites were more prone to corrosion attack where Cr distribution at the δ-γ interphase was nonuniform (Ref 10). From these observations it can be inferred that the weld metal is the weaker region of the weldment (Ref 12), and an assessment of its corrosion behavior is complicated by several factors. Though some literature on the effect of chemical composition and heat input on localized corrosion behavior is available (Ref 13-15), adequate information on the effect of alloying elements on uniform corrosion behavior is not available. The role of delta-ferrite in altering the uniform corrosion is not fully understood. As such, the present work deals with the effect of Cr and Mo additions on the uniform corrosion behavior of type 316 stainless steel weld metals in a deaerated 1 N H_2SO_4 solution containing 0.1g/L NH_4SCN.

M.G. Pujar, R.K. Dayal, and **T.P.S. Gill,** retired from Metallurgy and Materials Group (MMG) Indira Gandhi Centre for Atomic Research (IGCAR), Kalpakkam 603 102, India; and **S.N. Malhotra,** Metallurgical Engineering and Materials Science, Indian Institute of Technology (IIT), Bombay, Mumbai 400 076, India. Contact e-mail: mgpujar@rediffmail.com.

2. Experimental Procedure

2.1 Weld Metal Preparation

To prepare weld metal samples with known and controlled alloying element additions, a novel technique was used. This technique was termed *stationary arc tungsten inert gas* (SATIG) welding. With standardized welding conditions, tungsten inert gas (TIG) welding was carried out at a spot on the workpiece by keeping the arc stationary for a fixed duration of time, which gives the required weld metal penetration. The chief merit of this method is the ease of the addition of alloying elements during welding. The addition of alloying elements like Cr, Ni, and Mo was standardized using this technique, and it was found to be useful in achieving weld metal ferrite content values, which were quite reproducible. In the present study, 316 stainless steel plates of known chemical composition was used

for welding. A plate with dimensions of 100 × 100 × 25 mm was used to efficiently dissipate the heat during welding. This plate was thoroughly cleaned by wire brushing, degreased using a soap solution, and finally cleaned with acetone before welding. A 3 mm diameter tungsten electrode was ground using a tungsten electrode grinder to produce a tip vertex angle of 45°. At this vertex angle, the weld metal penetration was found to be maximum for a given set of welding conditions (Ref 16). Welding conditions were standardized by preparing weld metals without any alloying element addition. The welding conditions are given in Table 1. Ultra-high-purity argon gas was used for shielding the weld metal from oxidation. Argon gas was also used to flush any air present in the welding torch for 15 s prior to striking the arc. Every weld metal was prepared at the center of the plate to ensure uniform cooling conditions. The addition of alloying elements during welding was accomplished by inserting the accurately weighed chips, or wire pieces, of ultra-high-purity Cr and Mo through a ceramic rod to avoid any contamination. Before the addition of these elements, an arc was struck at a lower current value (~100 A) for 5 to 10 s, during which time the addition of the Cr and Mo was completed. Immediately after this, the welding current was raised to its standard value (~200 A) and was maintained there for the desired duration of time. To establish the weld metal penetration, the weld metals prepared without the addition of alloying elements were cut vertically, ground, and macroetched in a solution of 10 mL HNO_3 + 20 mL HCl + 30 mL water. The weld metal diameter was approximately 15 mm and, the penetration was 7 to 8 mm. The mean delta-ferrite content of the weld metal [ferrite number (FN)] prepared in this manner (without elemental addition) was found to be about 4.5 ± 0.2 FN. Five weld metal specimens of this type were prepared. To raise the ferrite content of these weld metals, accurately weighed high-purity Cr chips were added during welding. Additions of 80 and 200 mg of Cr resulted in weld metals with 6.3 ± 0.3 FN and 10.6 ± 0.4 FN, respectively. Similarly, additions of high-purity Mo wire (0.5 mm diameter) resulted in weld metals with 6.2 ± 0.4 FN (50 mg Mo) and 10.6 ± 0.6 (140 mg Mo), respectively.

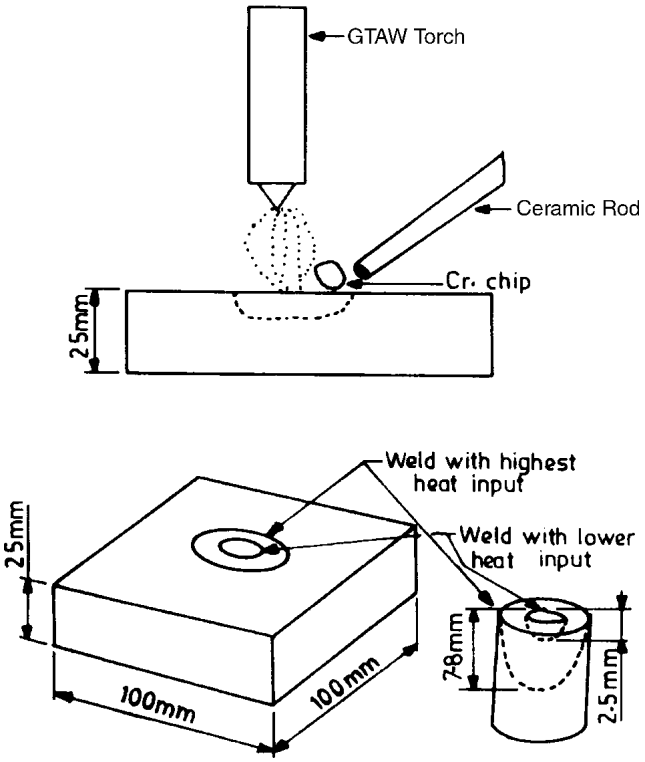

Fig. 1 Representation of gas tungsten arc welding (GTAW) welding by adding Cr chips (top). A 316 SS weld pad showing the location of the weld metal and the machined weld metal (bottom)

Table 1 Welding conditions for stationary arc tungsten inert gas welding

Welding current	200 A
Arc gap	3 mm
Argon flow rate	6 L/min
Welding voltage	20 V
Welding time	75 s

2.2 Change in the Heat Input

To alter the heat input, a different technique was adopted. Heat input was changed by changing the length of time that the arc strikes the workpiece. Four weld pads from each set, which were prepared by the technique described above, were used to obtain weld metals with different heat inputs that had the same chemical composition. The tungsten electrode tip was kept exactly at the center of the weld metal (one with the highest heat input). Except for the current, voltage, and arc strike time, all of the welding conditions were the same (Table 1). Stationary arc TIG welding (or arc striking) was carried out on these four weld metals for 5, 10, 15, and 20 s, respectively, at 100 A. The technique of adding the alloying elements during SATIG welding and the weld pad prepared in that way are shown in Fig. 1. Preliminary studies to observe the weld metal penetration were carried out as described earlier. The weld metals with different heat inputs (i.e., different arc strike-time values) had, on average, a penetration of 2.5 mm. The weld metal diameter was approximately 8 mm. Weld metal specimens were machined out from the plate carefully so as to avoid any base metal contamination (Fig. 1).

2.3 Calculation of the Heat Input Values

A standardized technique for the measurement of cooling curves during welding was adopted to determine the heat input values. Generally, the heat input (or energy input) term is applicable for those welding processes in which the welding torch is in continuous motion during welding, and heat input is given by:

$$\text{Heat input (kJ/mm)} = \frac{\text{Voltage (V)} * \text{Current (A)} * 60}{\text{Torch speed (mm/min)} * 1000}$$

As in the SATIG welding technique, with the torch stationary, an indirect method of calculation of heat input was followed. This method consisted of the measurement of cooling curves during autogenous welding (i.e., with a moving torch during welding) at known heat input values. From these measurements, a standard plot of heat input versus cooling time between two fixed temperatures was obtained, which was used as a calibration curve. Cooling curves were measured during SATIG welding for different arc strike times. The cooling curves obtained from these experiments yielded cooling times,

and from the above calibration curve, heat input values could be obtained. Because the TIG torch was stationary, the term *equivalent heat input* (EHI) was used.

2.4 Heat Input Measurement

To measure the cooling curves, a thermocouple made of tungsten/5wt.%rhenium to tungsten/26wt.%rhenium was used. One end of the thermocouple lead was connected to the strip chart recorder, while the other end was kept ready for plunging into the molten pool during welding. Autogenous welding at 100 A and 12 V, with a 3 mm arc gap was carried out on 25 mm thick plate at torch travel speeds of 125, 100, 75, and 50 mm/min, giving heat input values of 0.58, 0.72, 0.96, and 1.44 kJ/mm, respectively. One junction of the thermocouple was plunged into the molten pool as soon as the TIG torch passed by, while the strip chart recorder was maintained at the highest chart-rolling speed, thereby recording the cooling curve of the weld pool. In case of SATIG welding, the measurement of the cooling curves was accomplished in a similar manner by plunging the thermocouple end into the molten pool immediately after the arc was extinguished. From the standard chart of millivolts versus temperature for this thermocouple, cooling curves were obtained. The chemical compositions of the weld metals prepared at currents of 200 and 100 A with different heat input values were assumed to be the same for a given set of specimens. To know the chemical composition of these weld metals, a number of weld metals prepared at a current of 200 A were drilled (up to a depth of 3 mm) to collect weld metal chips. These were degreased and used for wet chemical analysis.

2.5 Delta-Ferrite Measurement

The delta-ferrite measurement was carried out using a Magne-Gage instrument, calibrated in accordance with the procedures laid out in AWS A4.2-74 (Ref 17). A total of 40 readings were taken to arrive at an average delta-ferrite value.

2.6 Microstructural Characterization

2.6.1 Chemical Etching Technique. Normally, austenitic stainless steel weld metals are etched in Murakami's reagent (a boiling solution of 10 g of potassium ferricyanide ($K_3Fe(CN)_6$) + 10 g of potassium hydroxide [KOH]) for about 3 min, wherein only the weld metal delta-ferrite is attacked. All of the weld metals, which are polished to fine diamond (1 μm) finish, were etched in this reagent, rinsed in distilled water, dried, and then observed in an optical microscope for delta-ferrite morphology.

2.6.2 Potentiostatic Etching Technique. This technique involved preparations of the weld metal specimen by polishing to a fine diamond finish, cleaning any grease and oil from the sample, and finally rinsing with double-distilled water. A solution of 0.5 M H_2SO_4 + 0.1 g/L NH_4SCN was prepared using double-distilled water. This solution was deaerated by passing ultra-high-purity argon gas through it for 1 h before immersion of the specimen. Throughout the etching experiments, the solution was continuously purged. After immersion, the specimen was cathodically cleaned by impressing a potential of –800 mV (i.e., with a saturated calomel electrode [SCE]) for 1 min. After surface cleaning, the potential at which etching was to be carried out was impressed immediately to avoid any corrosion attack at the open circuit potential (OCP). The time of etching was varied at every potential step depending upon the dissolution current. At every etching step, optical microscopic observations were made. Thus, the etching was carried in a potential range from –440 mV (SCE) until the specimen was passivated by changing the impressed potential in 20 mV increments.

Table 2 Chemical composition of the base and weld metals with different additions of alloying elements

		Weld metal, wt.%				
Element	Base metal	Without Cr/Mo addition	80 mg Cr	200 mg Cr	50 mg Mo	140 mg Mo
C	0.041	0.039	0.036	0.04	0.039	0.041
Si	0.60	0.61	0.60	0.59	0.60	0.57
Mn	1.44	1.44	1.47	1.42	1.40	1.44
S	0.018	0.020	0.019	0.018	0.019	0.020
P	0.020	0.020	0.023	0.027	0.025	0.027
Cr	17.19	16.81	17.96	18.71	16.80	16.63
Ni	10.76	10.61	11.07	11.39	11.07	11.23
Mo	2.46	2.42	2.40	2.82	4.16	5.83

Table 3 Weld metal specimen designations at different heat inputs

Heat input designation	WA	Cr1	Cr2	Mo1	Mo2
H1	WAH1	Cr1H1	Cr2H1	Mo1H1	Mo2H1
H2	WAH2	Cr1H2	Cr2H2	Mo1H2	Mo2H2
H3	WAH3	Cr1H3	Cr2H3	Mo1H3	Mo2H3
H4	WAH4	Cr1H4	Cr2H4	Mo1H4	Mo2H4
H5	WAH5	Cr1H5	Cr2H5	Mo1H5	Mo2H5

Table 4 Cr_{eq}/Ni_{eq} ratios by using different formulas

Weld metal	Cr_{eq}/Ni_{eq}		
	Suutala (a)	DeLong (b)	WRC-92 (c)
WA	1.71	1.50	1.53
Cr1	1.74	1.50	1.57
Cr2	1.79	1.58	1.61
Mo1	1.83	1.58	1.61
Mo2	1.96	1.66	1.69

(a) Suutala (Ref 24): $Cr_{eq}/Ni_{eq} = \dfrac{Cr + 1.37Mo + 1.5Si + 2Nb + 3Ti}{Ni + 0.31Mn + 22C + 14.2N + Cu}$;

(b) DeLong (Ref 25): $Cr_{eq}/Ni_{eq} = \dfrac{Cr + Mo + 1.5Si + 0.5\,Nb}{Ni + 0.5Mn + 30(C + N)}$;

(c) Kotecki and Siewert (Ref 26): $Cr_{eq}/Ni_{eq} = \dfrac{Cr + Mo + 0.7\,Nb}{Ni + 35C + 20N + 0.25Cu}$.

Table 5 Delta-ferrite contents for weld metals with different chemical compositions and heat inputs in FN

Heat input	WA	Cr1	Cr2	Mo1	Mo2
H1	3.4 ± 0.4	9.0 ± 0.2	14.2 ± 0.4	8.3 ± 0.2	9.6 ± 0.3
H2	4.0 ± 0.3	9.5 ± 0.5	10.6 ± 0.4	6.9 ± 0.2	9.2 ± 0.6
H3	5.0 ± 0.1	9.4 ± 0.2	10.3 ± 0.6	7.0 ± 0.3	8.9 ± 0.3
H4	6.5 ± 0.2	8.7 ± 0.2	9.1 ± 0.6	8.7 ± 0.5	8.7 ± 0.3
H5	4.2 ± 0.4	6.8 ± 0.6	12.1 ± 1.0	6.1 ± 0.5	13.3 ± 0.6

2.7 Anodic Polarization Experiments

Anodic polarization experiments were followed as per the instructions given in the standard practice prescribed in the ASTM G5-87 standard (Ref 18). The corrosion of stainless steels occurs in service due to a passive-to-active transition involving a change in the service conditions. An acidified ammonium thiocyanate solution is found to be useful in simulating such a moderately oxidizing medium in which the active-passive transition of the metal could be easily studied. Ammonium thiocyanate also reduced the effect of concentration polarization and was found to be stable over the entire potential range used in these studies (Ref 19). All the solutions were purged with oxygen-free argon gas for 1 h before beginning any experiment. All the electrode potentials were measured against an SCE. The cylindrical specimen was mounted and polished to a fine diamond finish and then was cleaned. The specimen was then immersed in the deaerated solution such that the distance between the tip of the Luggin-Haber probe and the specimen surface was about 3 to 4 mm. After the attainment of a stable OCP, cathodic polarization was carried out from the OCP to –1000 mV (SCE). Subsequently, the specimen surface (without removing the sample from the cell) was cleaned of any hydrogen bubbles, and a time interval of 15 min was allowed for the specimen to attain its OCP value. After this, another anodic polarization experiment

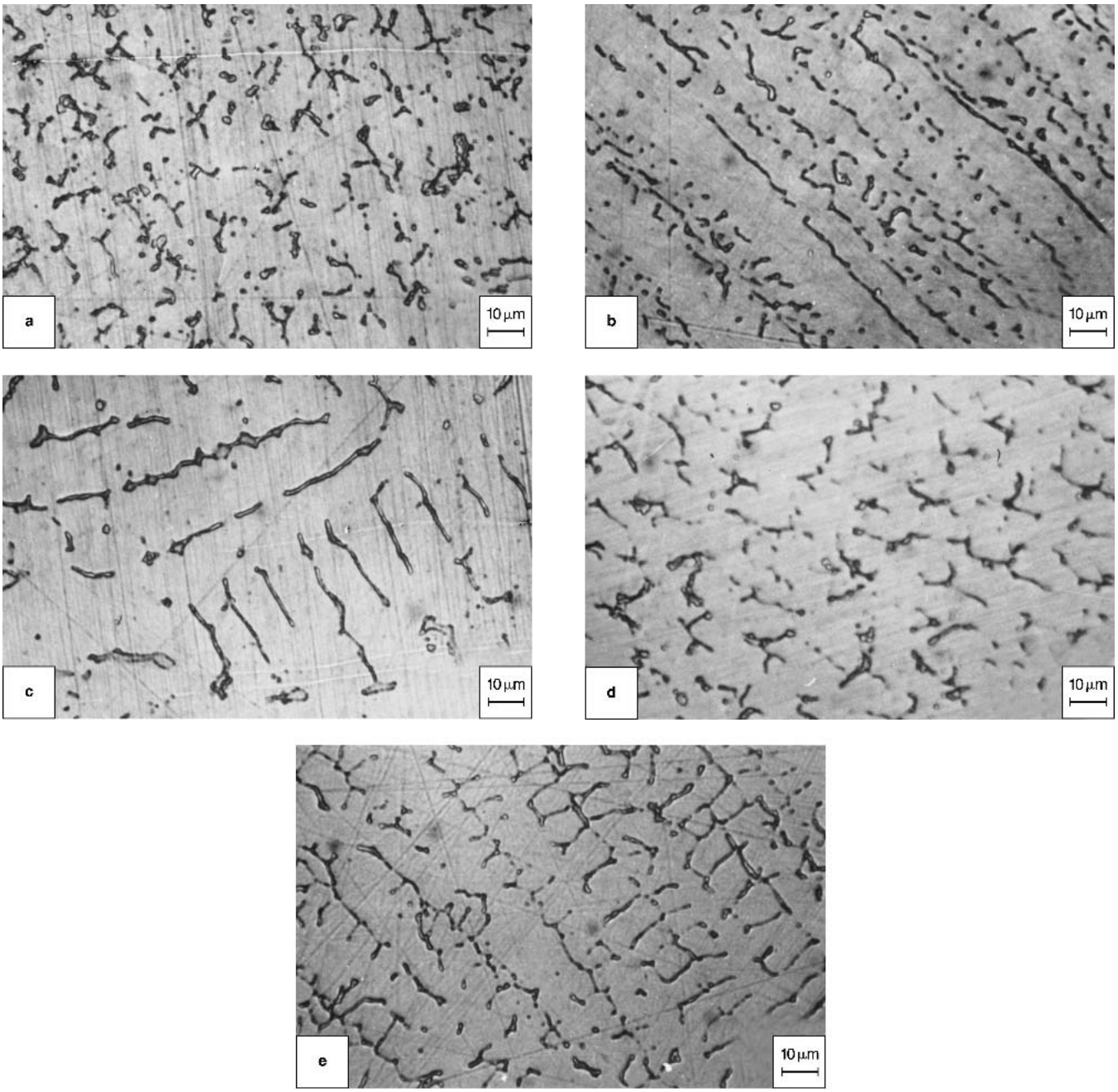

Fig. 2 Photomicrographs of weld metal WA at heat inputs (a) H1, (b) H2, (d) H3, (e) H4, and (c) H5 in as-welded condition. The weld metal was etched in Murakami's reagent.

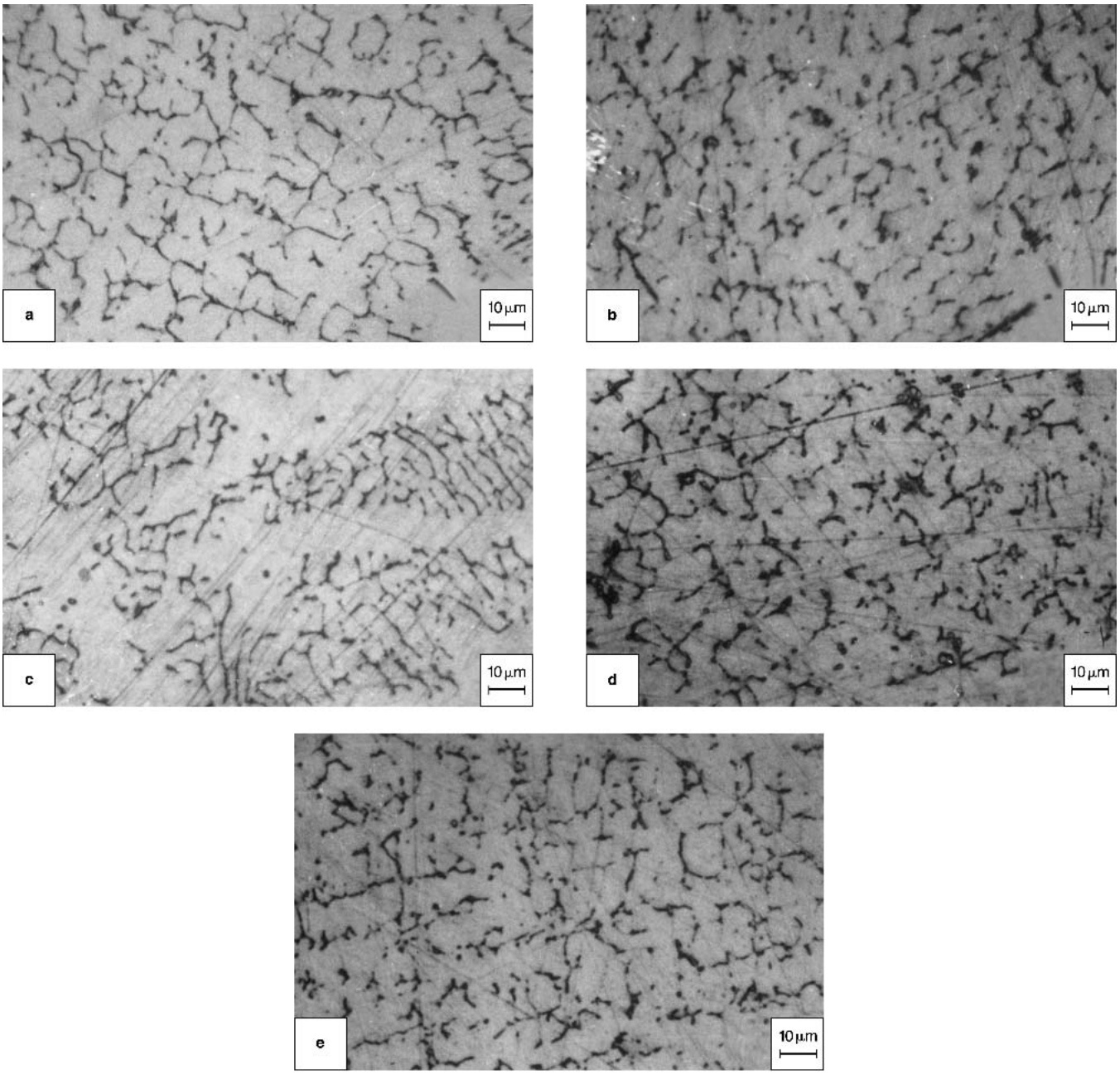

Fig. 3 Photomicrographs of weld metal Cr1 at heat inputs (a) H1, (b) H2, (d) H3, (e) H4, and (c) H5 in as-welded condition. The weld metal was etched in Murakami's reagent.

was carried out from OCP to +1000 mV (SCE). Generally, all the specimens were found to be in the transpassive region at this potential value. Anodic and cathodic Tafel slopes, peak and passive current density values, primary passivation potentials (E_{pp}), range of passivity, and transpassive potential values were obtained from these studies.

2.8 Polarization Resistance Studies

The apparatus and other parts of the experimental setup for this study were the same as described in the previous section. The standard procedure for carrying out a potentiodynamic polarization resistance (PR) experiment was followed as per the practice described in ASTM G59-91 (Ref 20). The corrosion current calculation employing PR data involved cathodic and anodic Tafel slopes. Because these Tafel slopes were obtained at higher overpotentials during potentiodynamic cathodic and anodic polarization experiments using a scan rate of 10 mV/min, polarization experiments were also performed at 10 mV/min. The maximum potential scan range was fixed at +30 mV from the OCP of the specimen. The electrolyte was a deaerated solution of 0.5 M H_2SO_4 + 0.1 g/L NH_4SCN. After an immersion time of 1 h, the OCP was measured. The scan was initiated from –30 mV (SCE), which was active to the OCP and was completed at +30 mV (SCE) noble to the OCP. The potential scan data so obtained were plotted as current density (in microamperes per square centimeter) against ΔE (i.e., the overpotential in either direction). From the slopes of

the ΔE versus current density plots, the PR was obtained, which was used to calculate the corrosion currents.

2.9 Three-Point Method Studies

All the experiments were carried out using the same experimental setup and electrolytes, as well as the same procedures used in the potentiodynamic polarization and PR studies. Because the scan rate is the most important aspect of these experiments, a scan rate of 1 mV/min was used to achieve a steady state. The specimen was polarized cathodically from the OCP until ΔE equaled 30 mV (SCE), where $\Delta E = E - E_{corr}$. Corrosion rates and Tafel slopes were calculated at every potential as per the standard procedures (Ref 21, 22).

3. Results and Discussion

3.1 Heat Input Values

Generally, cooling time is calculated between 800 and 500 °C, as it predicts the heat-affected zone hardness more accurately. However, this temperature interval is selected based on some empirical equations and is not a standard practice (Ref 23). In these experiments, a temperature interval between 1000 and 500 °C was chosen for determining the cooling times. The calculated cooling times for autogenous welds prepared at the 100 A current at different heat inputs were plotted to give the "best fit" to the curve:

Heat input (kJ/mm) = 0.23 × (Cooling time, s) – 0.27

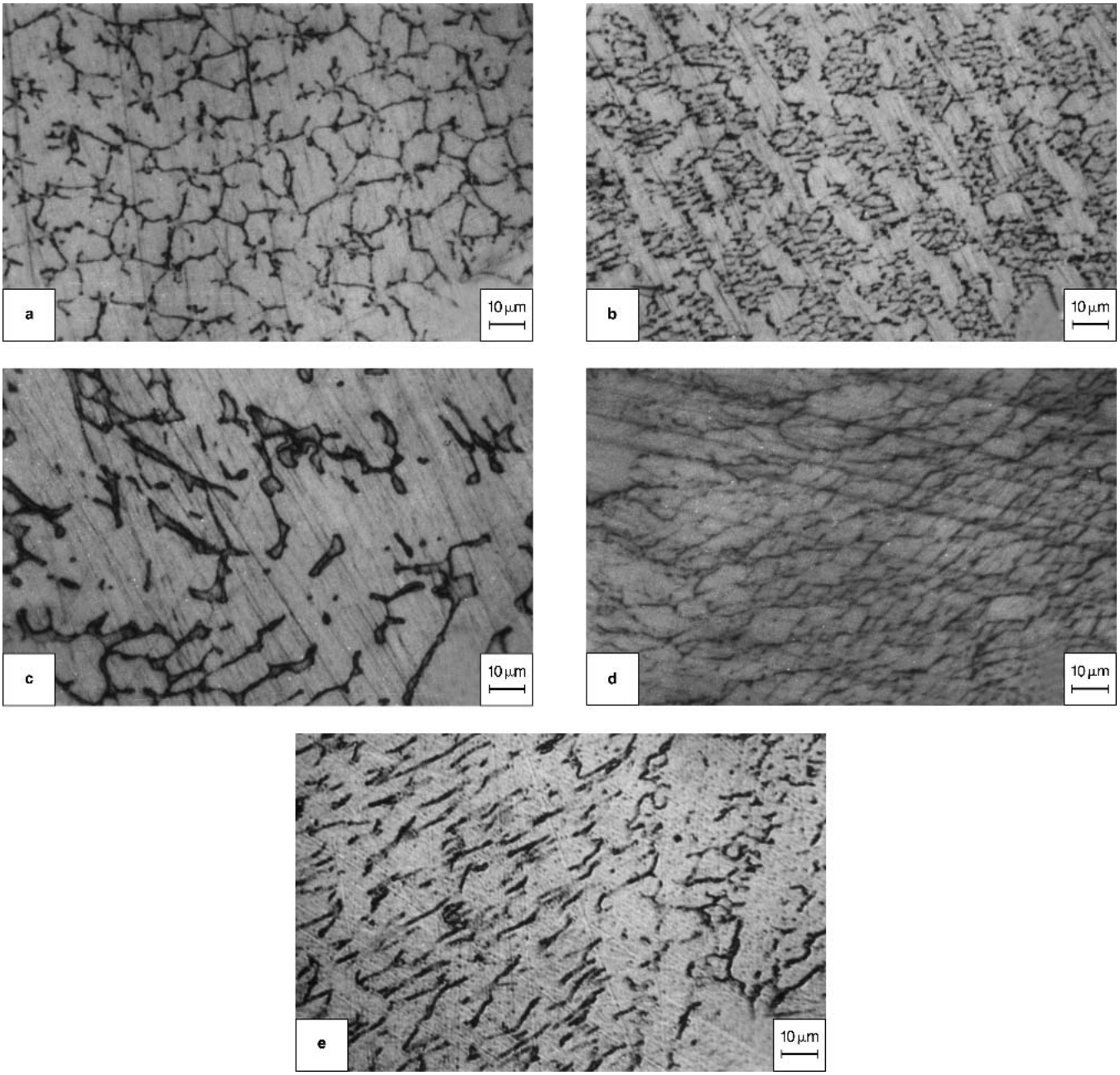

Fig. 4 Photomicrographs of weld metal Cr2 at heat inputs (a) H1, (b) H2, (d) H3, (e) H4, and (c) H5 in as-welded condition. The weld metal was etched in Murakami's reagent.

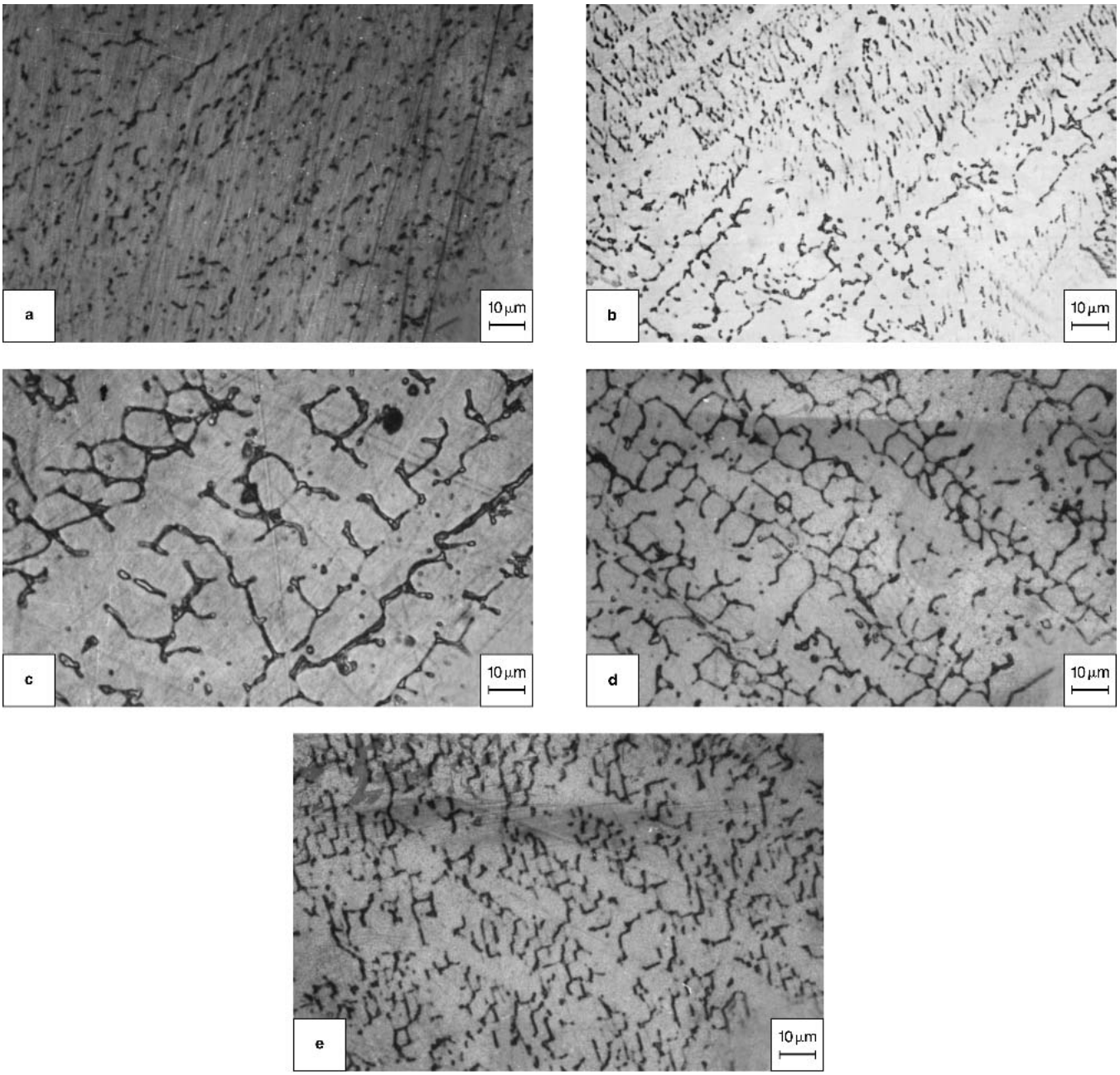

Fig. 5 Photomicrographs of weld metal Mo1 at heat inputs of (a) H1, (b) H2, (d) H3, (e) H4, and (c) H5 in as-welded condition. The weld metal was etched in Murakami's reagent.

Using the conditions of the SATIG welding parameters and the same plate thickness, heat input values were calculated using this equation. These heat input values are termed the EHI as the TIG torch is stationary. The EHI values for 5, 10, 15, and 20 s arc strike times were calculated by using this equation, and were found to be 0.36, 0.56, 0.85, and 1.00 kJ/mm, respectively.

3.2 Chemical Composition of the Weld Metals

The chemical compositions of all of the weld metals along with the base metal are given in Table 2. It was noted that additions of 80 and 200 mg of pure Cr chips during welding raised the weld metal Cr content from 16.81 wt.% (without addition) to 17.96 wt.% (a 1.16 wt.% increase) and 18.71 wt.% (a 1.9 wt.% increase), respectively. Similarly, additions of 50 and 140 mg of Mo changed the initial concentration of Mo (2.42 wt.% without any addition) to 4.16 wt.% (a 1.74 wt.% increase) and 5.83 wt.% (a 3.41 wt.% increase), respectively. The C, N, and Ni concentrations were unchanged as a result of Cr and Mo additions during welding.

The specimens without any elemental addition were designated as WA. The specimens with 80 and 200 mg of Cr added were designated as Cr1 and Cr2, respectively. Similarly, the specimens with 50 and 140 mg of Mo added were designated as Mo1 and Mo2, respectively. The heat input values of 0.36, 0.56, 0.85, and 1.00 kJ/mm were designated as H1, H2, H3, and H4, respectively. The designations of all specimens with dif-

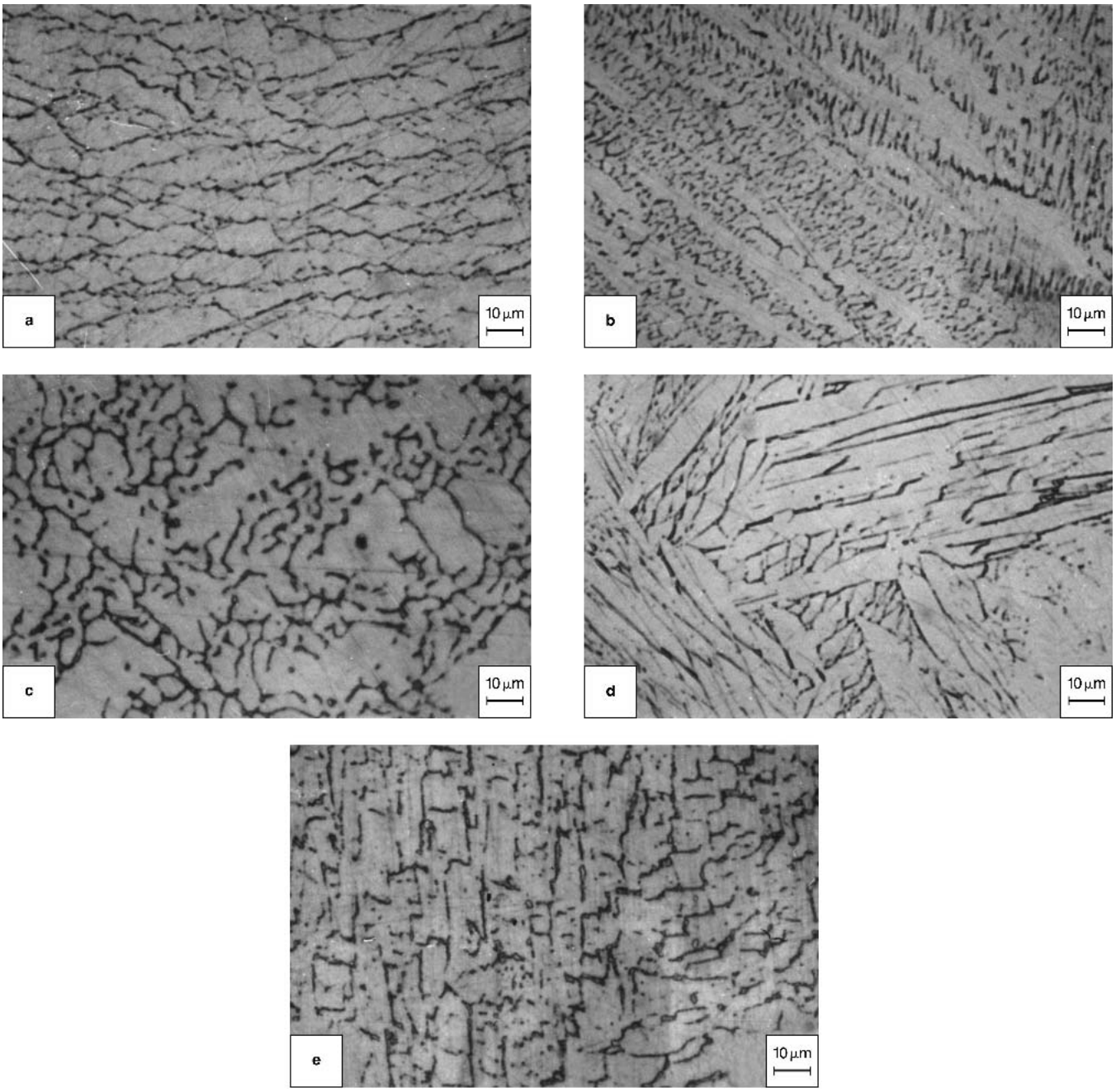

Fig. 6 Photomicrographs of weld metal Mo2 at heat inputs (a) H1, (b) H2, (d) H3, (e) H4, and (c) H5 in as-welded condition. The weld metal was etched in Murakami's reagent.

ferent heat inputs are given in Table 3 and are used in the remaining sections of this article. The term *Cr-added weld metals* signifies WA, Cr1, and Cr2 specimens with increasing Cr contents. Similarly, the term *Mo-added weld metals* signifies WA, Mo1, and Mo2 specimens with increasing Mo contents.

3.3 Mode of Solidification and Delta-Ferrite Contents

The mode of solidification can be determined from the Cr_{eq} to Ni_{eq} ratios. To ascertain the mode of solidification, the Cr_{eq} to Ni_{eq} ratios were determined using formulas proposed by Suutala (Ref 24), DeLong (Ref 25), and Kotecki and Siewert (Ref 26). It should be noted that coefficients of some of the austenitizers and ferritizers, such as C, N, Mn, Mo, and Nb, were different in these formulas and yielded slightly different ratios. These values have been presented in Table 4. It was found that the ratios for all of the specimens were higher than 1.5, signifying that the primary mode of solidification in the weld metals was ferritic. The values of the delta-ferrite contents of weld metals with different heat inputs have been given in Table 5. It was noted that the ferrite contents of the welds prepared with the lowest heat input (highest cooling rate) were, in general, higher compared with those of the other welds. However, the variation of delta-ferrite values observed was less than ±2 FN.

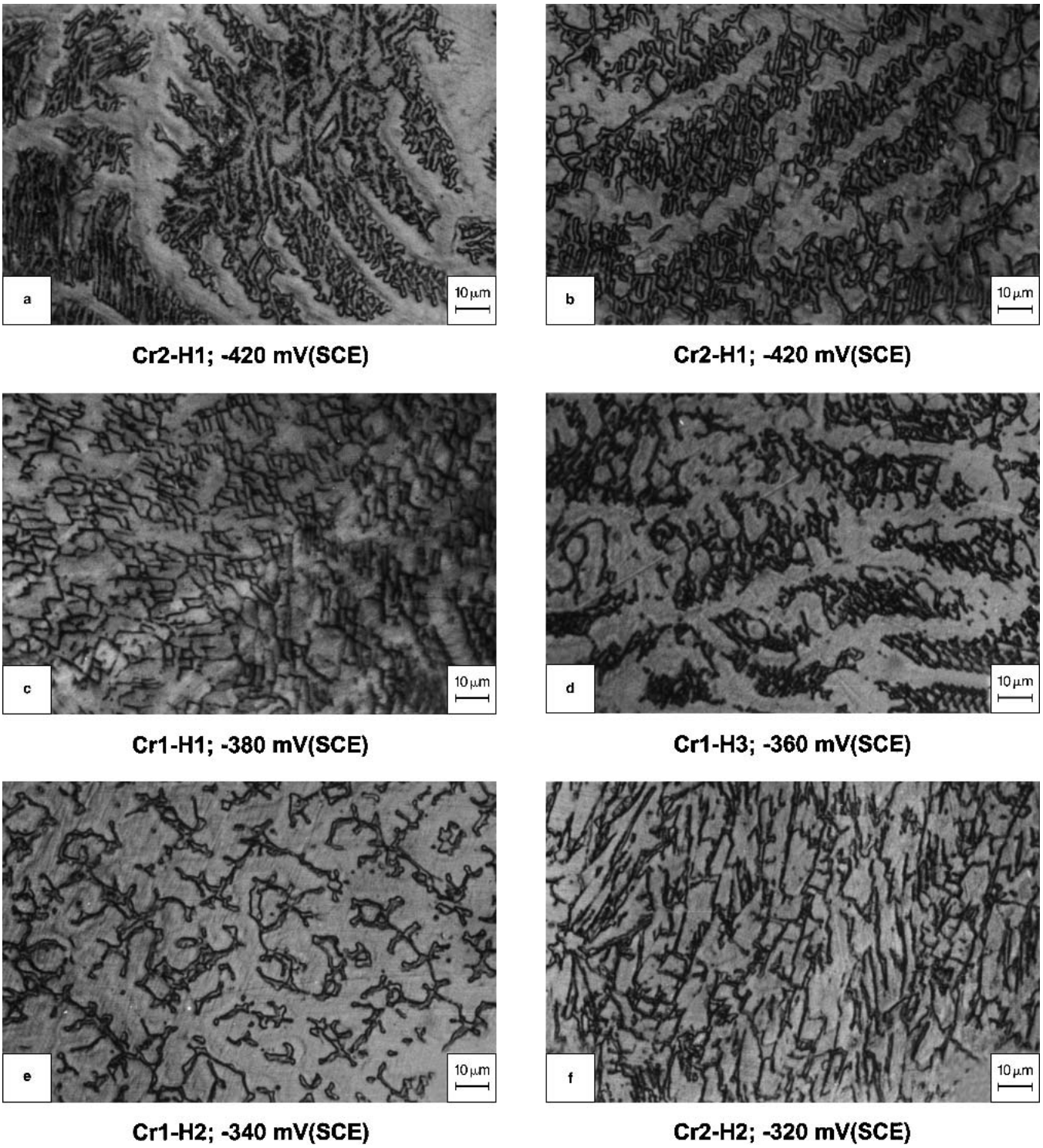

Fig. 7 (a-f) Photomicrographs after potentiostatic etching in deaerated 0.5 M H_2SO_4 + 0.1 g/L NH_4SCN at different active potentials. The weld metal specimens had 16.81 to 18.71 wt.% Cr added.

3.4 Microstructural Studies

3.4.1 Chemical Etching. The microstructure of the solidified austenitic stainless steel welds was characterized according to the morphology of the ferrite present. The development of the final microstructure is dependent on several welding and metallurgical conditions. Detailed information about the ferrite morphologies, and their classifications, has been reported elsewhere (Ref 27, 28). Structures solidified as the primary ferrite exhibit a wider range of ferrite morphologies and depend on the ratio of Cr_{eq} to Ni_{eq} (Ref 29, 30). Figure 2(a) to (d) shows the ferrite morphologies observed in the weld metal WA at different heat inputs. The ferrite morphology was extremely fine at H1, which gradually coarsened due to the increase in the heat input. The ferrite morphology observed in these specimens could be categorized as skeletal or vermicular ferrite (3 < FN

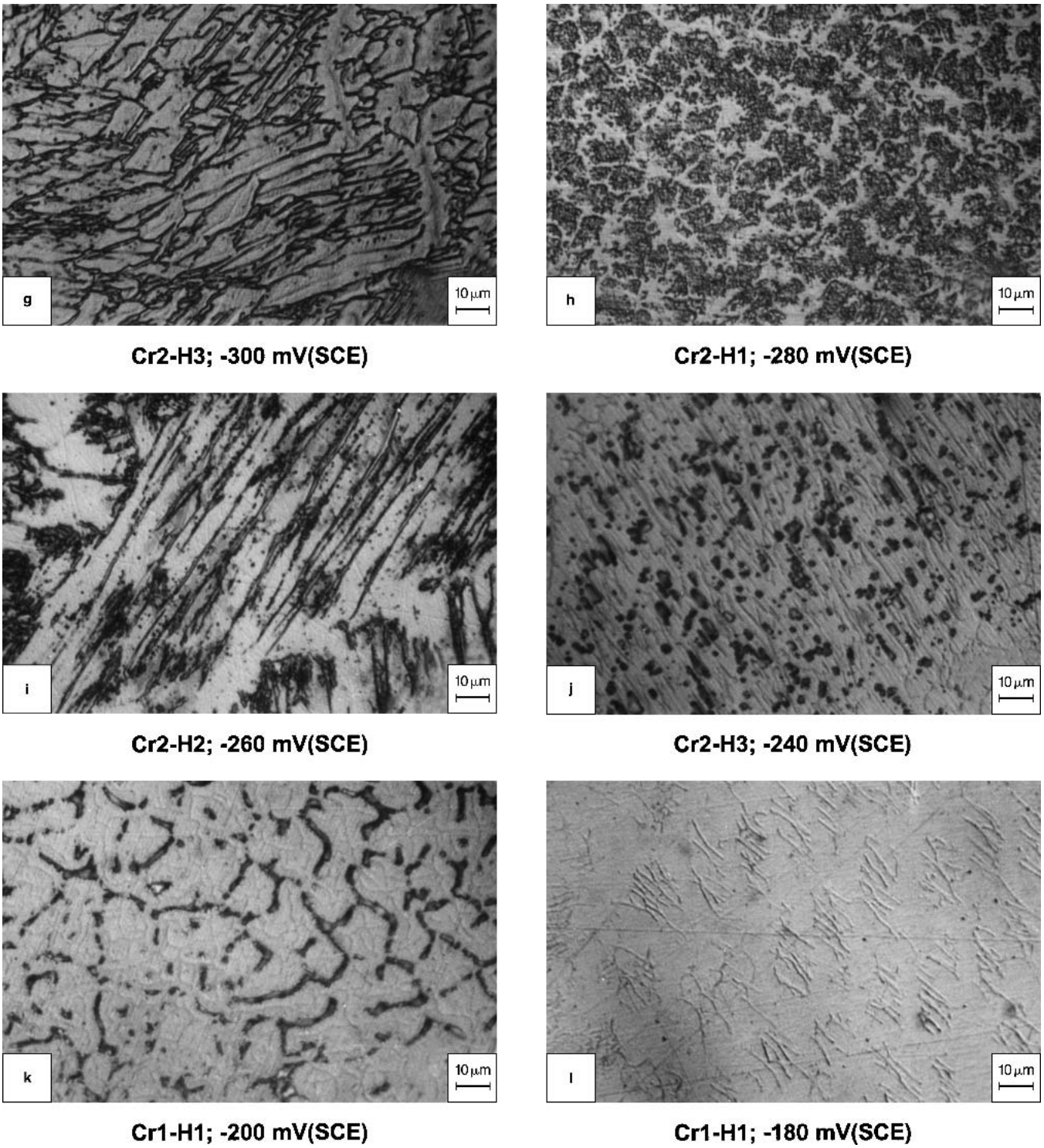

Fig. 7 cont. (g-l) Photomicrographs after potentiostatic etching in deaerated 0.5 M H_2SO_4 + 0.1 g/L NH_4SCN at different active potentials. The weld metal specimens had 16.81 to 18.71 wt.% Cr added.

< 7). Photomicrographs (Fig. 2b, and d) showed that ferrite grew in the solidification direction (SD). Also, Fig. 2(a) and (c) showed that ferrite grew at an angle to the SD. The ferrite morphology observed for specimens Cr1 in Fig. 3(a) to (d), and for Cr2 in Fig. 4(a) to (d), was essentially skeletal with a continuous interconnected network. The amount of ferrite in these specimens varied from 9 to 14 FN. In Fig. 4(b) and (d), ferrite laths were observed that were correlated with the incomplete transformation of ferrite to austenite. Figure 5(a) to (d) and Fig. 6 (a) to (d) show the ferrite morphology for specimens Mo1 and Mo2, respectively. The ferrite was observed to be lathy with an interconnected network. Growth of Widmanstatten austenite can be seen in Fig. 6(d), and is attributed to the increased cooling time with the increase in heat input that allowed the nucleation and growth of austenite within the ferrite. This also indicated that the compositions in the ferrite and

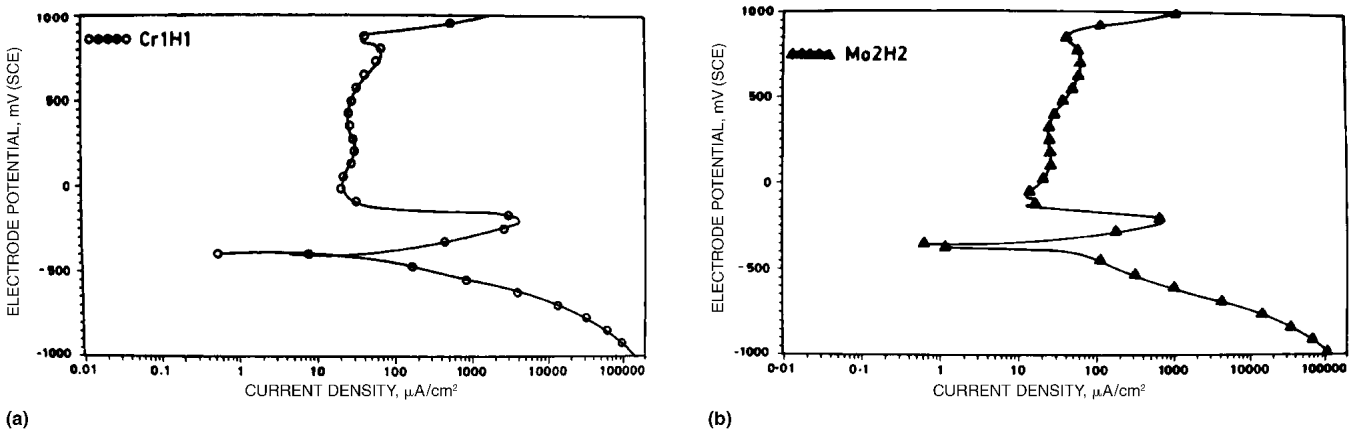

Fig. 8 Typical potentiodynamic anodic polarization curves for weld metal specimens Cr1H1 and Mo2H2 in deaerated 0.5 M H_2SO_4 + 0.1 g/L NH_4SCN

Table 6 Best-fit equations for *X* where *X* = Cr + (B∗Mo) + (C∗FN)

Heat input	Peak C.D.	Range of passivity	E_{pp}	Corrosion rate
H1	X = Cr + 10.62Mo + 0.98FN (r = −0.97)	X = Cr + 1.27Mo (r = 0.87)	X = Cr + 1.94Mo + 0.78FN (r = −0.93)	X = Cr + 2.06Mo + 1.12FN (r = −0.90)
H2	X = Cr + 13.89Mo + 3.09FN (r = −1.00)	X = Cr + 1.07Mo (r = 0.90)	X = Cr + 2.71Mo + 1.04FN (r = −0.82)	X = Cr + 2.96Mo + 1.05FN (r = −1.00)
H3	X = Cr + 11.22Mo + 1.40FN (r = −0.98)	X = Cr + 1.96Mo (r = 0.88)	X = Cr + 1.87Mo + 0.91FN (r = −0.94)	X = Cr + 2.21Mo + 0.97FN (r = −0.74)
H4	X = Cr + 7.00Mo + 1.00FN (r = 0.98)	X = Cr + 1.12Mo (r = 0.85)	X = Cr + 0.89Mo + 0.27FN (r = −0.95)	X = Cr + 0.62Mo + 5.00FN (r = −0.96)
H5	X = Cr + 11.30Mo + 0.79FN (r = −0.90)	X = Cr + 1.09Mo (r = 1.00)	X = Cr + 1.00Mo + 1.00FN (r = −0.96)	X = Cr + 0.73Mo − 0.09FN (r = −0.92)

austenite must be fairly uniform as extensive diffusion is involved during the process of transformation.

3.4.2 Potentiostatic Etching. The weld metal chemical composition was very similar except for the Cr contents in Cr1 and Cr2, and the Mo contents in Mo1 and Mo2. Although the small variations in the Cr contents (Cr1 and Cr2) and Mo contents (Mo1 and Mo2) did not show significant differences in their microstructural features, their overall corrosion properties might vary. Photomicrographs after the potentiostatic etching of Cr1 and Cr2 specimens are shown in Fig. 7(a) to (l). The photomicrographs in Fig. 7(a) to (d) showed corrosion attack on delta-ferrite; however, the areas immediately enveloping ferrite were protected and appeared bright (Fig. 7a). Austenite was lightly attacked (Fig. 7a-d). In the potential range of –420 to –360 mV (SCE), ferrite laths were clearly etched. As the etching potential became more anodic, attack on the δ-γ interface boundaries was observed (Fig. 7e). Figure 7(h) showed microstructural features wherein austenite was predominantly attacked, revealing very fine features. Etching at –240 mV (SCE) (Fig. 7i) revealed the dissolution of the interdendritic zones. This micrograph showed that there were many similar regions that had resisted the corrosion attack, signifying that these regions had higher Cr concentrations. It is well known that the Cr distribution is nonuniform across the δ-γ interface boundaries. Figure 7(k) shows the delta-ferrite in the passive condition after etching at –200 mV (SCE). It was observed that the areas of interdendritic austenite that were far removed from delta-ferrite showed high corrosion attack (Fig. 7k). These regions had the lowest Cr contents and, hence, dissolved actively at such a noble potential (–200 mV [SCE]). At –180 mV (SCE), the specimen passivated completely, and the skeletal ferrite was seen on the dull background of austenite.

3.5 Electrochemical Corrosion Behavior

Typical cathodic and anodic polarization curves of Cr1 at H1 and Mo2 at H2 are shown in Fig. 8(a) and (b), respectively. Similar polarization curves were obtained for Cr2, Mo1, and Mo2 specimens with different heat inputs. Anodic polarization curves showed a single well-defined peak, and dissolution of the ferrite was not observed on the anodic curve due to the dynamic nature of the experiment and because sufficient time was not allowed at every potential. Electrochemical parameters, such as critical anodic current density, range of passivity, E_{pp}, and corrosion rate, are strongly dependent on the alloy chemistry. In austenitic stainless steel weld metals, delta-ferrite is dispersed in the austenitic matrix. The addition of Cr and Mo to the weld metal enriches the delta-ferrite content of the weld metal with these elements, simultaneously raising the level of microsegregation of these elements at the δ-γ interface boundaries. Therefore, the ferrite content is expected to have a strong bearing on the electrochemical parameters. To study the role of delta-ferrite alongside that of Cr and Mo, a different method of data analysis was followed.

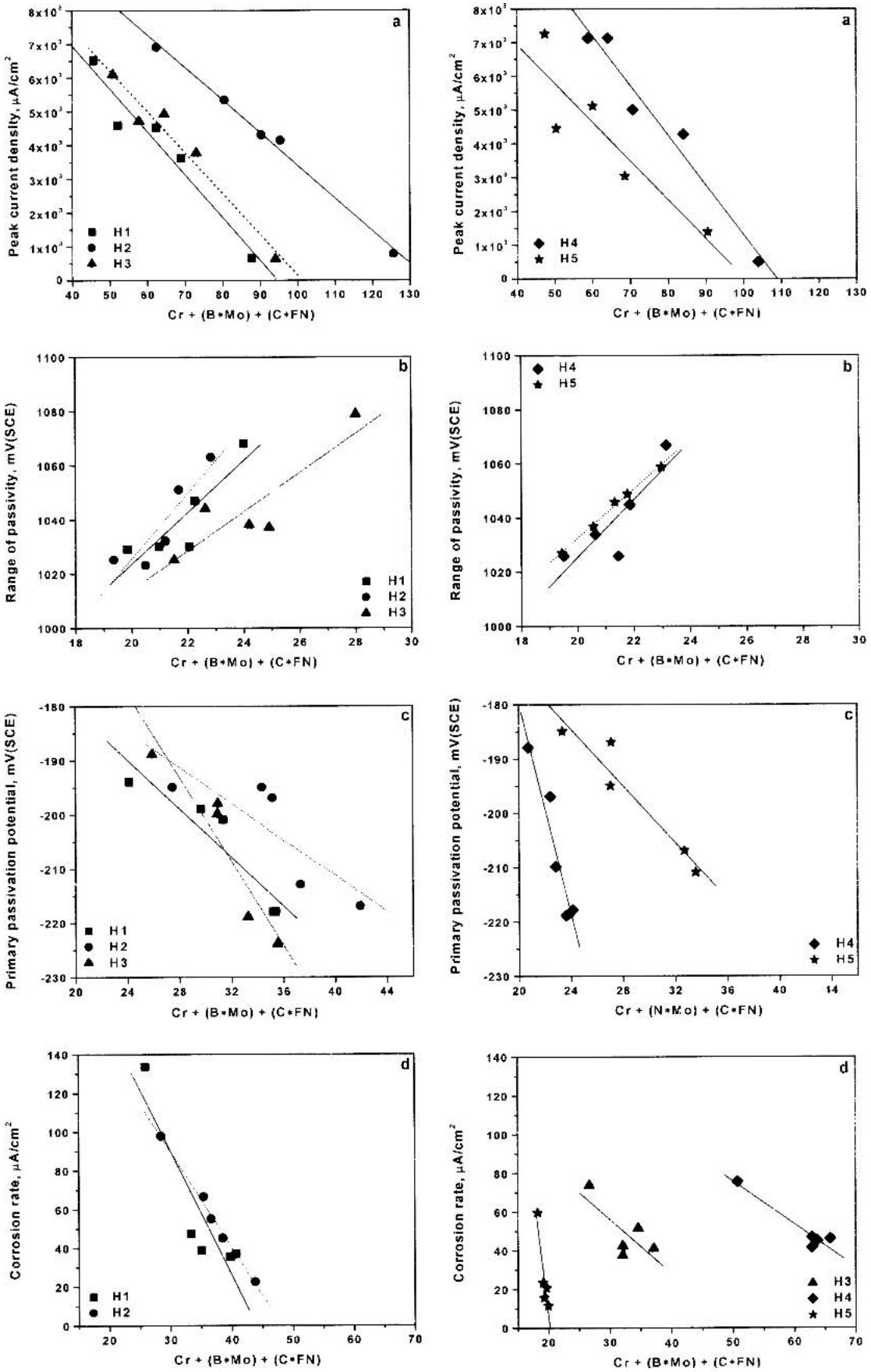

Fig. 9 (a) Plots of peak current density, (b) range of passivity, (c) E_{pp}, and (d) corrosion rate (TPM), as a function of Cr + (B × Mo) + (C × FN)

3.6 Data Analysis

To arrive at a meaningful interpretation, a new method of data analysis was adopted. A combined independent variable was defined as $X = Cr + (B \times Mo) + (C \times FN)$, where Cr and Mo were the actual concentrations of Cr and Mo in a given weld metal, FN was the ferrite content of the same weld metal, and B and C were coefficients of Mo and ferrite. Analysis of corrosion data with respect to this variable helps in studying the combined effects of the alloying elements and ferrite content on the electrochemical parameters. An iterative method was used to arrive at the optimum values of the coefficients. Accurate values of B and C were determined by assigning different values to B (with C kept constant) and C (with B kept constant), and, after repeated iterations, values that resulted in the highest correlation coefficient were selected. The values of X at every heat input that yielded the highest r value (Table 6) were plotted against the corresponding electrochemical parameters (Fig. 9a-d).

It is evident (Fig. 9a) that the critical anodic current density sharply decreased as a function of X. From the equations given in Table 6, it was inferred that, among the major alloying elements, Mo was found to be more effective in inhibiting the critical anodic current density. The coefficients of Mo (Table 6) suggested that Mo had overwhelming importance in decreasing the critical anodic current density compared with Cr and ferrite. It has been reported that the addition of Mo (0 to 2 wt.%) decreased the critical anodic current density of a 12 wt.% Cr steel in sulfuric acid (Ref 31). Lizlovs (Ref 32) has reported a decrease in the critical anodic current density by a factor of 12 to 13 when 3 wt.% Mo was added to a 17 wt.% Cr stainless steel. An addition of 8 wt.% Mo was shown to passivate an 18Cr stainless steel spontaneously in 1 N sulfuric acid (Ref 33).

The range of passivity values when plotted against X showed (Fig. 9b) an initially slower increase followed by a sharp rise with an increase in X. Molybdenum was slightly more effective than Cr in raising the range of passivity values; however, it seemed that ferrite did not play a significant role. The increase in Cr is known to shift the E_{pp} values in the active direction (Ref 34), but Mo was found to be more beneficial as it not only shifts the E_{pp} values in the active direction but simultaneously ennobles the OCP (Ref 34), thereby shrinking the entire active peak.

It is well known that, for a given reduction curve, the values of the E_{pp} and the critical anodic current density determine whether the alloy will spontaneously passivate (Ref 35). The E_{pp} values decreased with an increase in X (Fig. 9c), and the influence of Mo was much stronger than that of Cr and ferrite. A similar effect was observed by Bond and Lizlovs (Ref 36). In their work, the anodic polarization behavior of a 20Cr-39Ni stainless steel with various additions of Mo (0 to 5 wt.%) was studied in hydrochloric acid.

The corrosion rates obtained by the PR technique were found to be slightly overestimated compared with the rates obtained by the other two techniques (Table 7). It was reported by Yau and Streicher (Ref 37) that the corrosion rates obtained by the three-point method (TPM) correlated well with those obtained by the mass-loss method, and better than the ones obtained by the PR technique. Therefore, the corrosion rates obtained by the TPM were used for analysis. The plot of the corrosion rates against X showed a continuous decreasing trend with increasing values of X (Fig. 9d). Molybdenum was found to be doubly effective compared with Cr. Molybdenum decreases the corrosion rates of an alloy by stifling the anodic dissolution of the alloy (Ref 34), a fact that was observed where specimens containing Mo showed decreased mass loss in the potentiostatic dissolution studies. Molybdenum, owing to its noble OCP, is enriched at the surface, suppressing active dissolution of the alloy further (Ref 38, 39). It must be emphasized that the importance of Cr is indisputable in increasing the passivability of the alloy. This was demonstrated by Sugimoto and Sawada (Ref 40), who reported that the decrease in critical anodic current density values by Mo addition was gradual and not very substantial until an adequate amount of Cr was added to the alloy. In the active potential range, Mo inhibits the dissolution of the alloy due to its noble OCP (Ref 41), but beyond the E_{pp}, Mo suffers from transpassive dissolution (Ref 42), which is prevented by increasing Cr concentration. From the data shown in Table 6, it is clear that delta-ferrite plays a definite and favorable role in altering the electrochemical parameters of the alloy, and that it is equivalent to that of Cr.

Table 7 Corrosion rates by three different techniques for weld metals at H1

Weld metal	Corrosion rate, μA/cm²		
	Cathodic Tafel slope extrapolation	PR	TPM
WA	66.29	233.43	134.49
Cr1	45.75	110.91	47.49
Cr2	47.71	54.79	37.15
Mo1	40.47	28.04	39.09
Mo2	15.09	35.67	35.82

Note: PR, polarization resistance; TPM, three-point method

3.7 Effect of Heat Input

The best-fit equations obtained by plotting X against the various electrochemical parameters are shown in Table 8. It

Table 8 Best-fit equations obtained by plotting electrochemical parameters against X

Heat input	Peak CD	RP	E_{pp}	Corrosion rate
H1	$-127(X) + 12{,}033$	$9.58(X) + 848.60$	$-2.24(X) - 136.16$	$-7.51(X) + 313.04$
H2	$-7(X) + 13{,}101$	$12.14(X) + 831.33$	$-1.66(X) - 144.66$	$-4.96(X) + 237.52$
H3	$-121(X) + 12{,}276$	$7.24(X) + 868.66$	$-3.86(X) - 84.93$	$-2.69(X) + 138.62$
H4	$-154(X) + 16{,}650$	$10.78(X) + 809.68$	$-9.69(X) + 14.22$	$-2.22(X) + 187.62$
H5	$-115(X) + 11{,}525$	$9.19(X) + 848.60$	$-2.60(X) - 122.12$	$-26.45(X) + 535.37$

Note: CD, current density; RP, range of passivity

should be noted that within the range of heat inputs studied, the electrochemical parameters did not show any particular trend with heat input. To study the relation between the E_{pp} and corrosion rates, best-fit equations obtained for the E_{pp} and corrosion rates at different heat inputs (H1 to H4), were used to calculate the E_{pp} and corrosion rate values at fixed values of X. Those values of X were used which resulted in E_{pp} values that were actually observed experimentally and were realistic. The linear plots (Fig. 10) of corrosion rates and the corresponding E_{pp} values showed decreasing slopes with increasing heat inputs. The best-fit equations were as follows:

$$H1 \rightarrow \text{Corrosion rate} = 3.35\,(E_{pp}) + 770 \quad r = 1.00$$
$$H2 \rightarrow \text{Corrosion rate} = 2.98\,(E_{pp}) + 670 \quad r = 1.00$$
$$H3 \rightarrow \text{Corrosion rate} = 0.70\,(E_{pp}) + 198 \quad r = 1.00$$
$$H4 \rightarrow \text{Corrosion rate} = 0.23\,(E_{pp}) + 184 \quad r = 1.00$$

These equations suggested that the corrosion rates were dependent on the E_{pp} values only at lower heat inputs, and with an increase in heat input, the corrosion rates became almost independent of the E_{pp}. It should also be noted that as the E_{pp} values became more and more active, the corrosion rates decreased rapidly. This is directly related to the increased rate of passivation discussed previously.

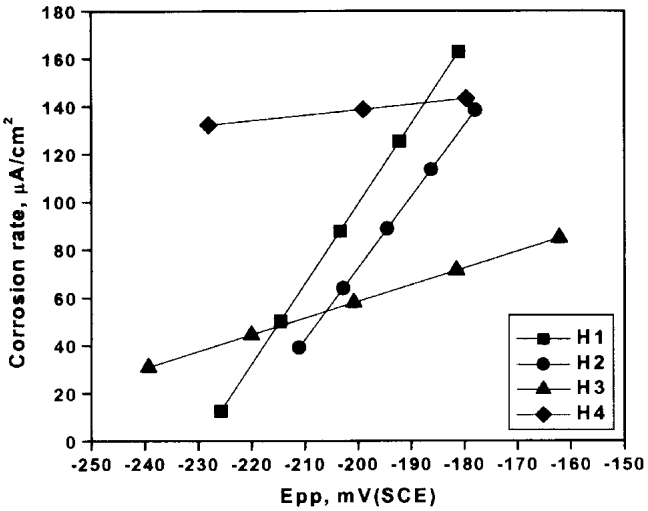

Fig. 10 Plot showing the correlation between the corrosion rate and E_{pp}

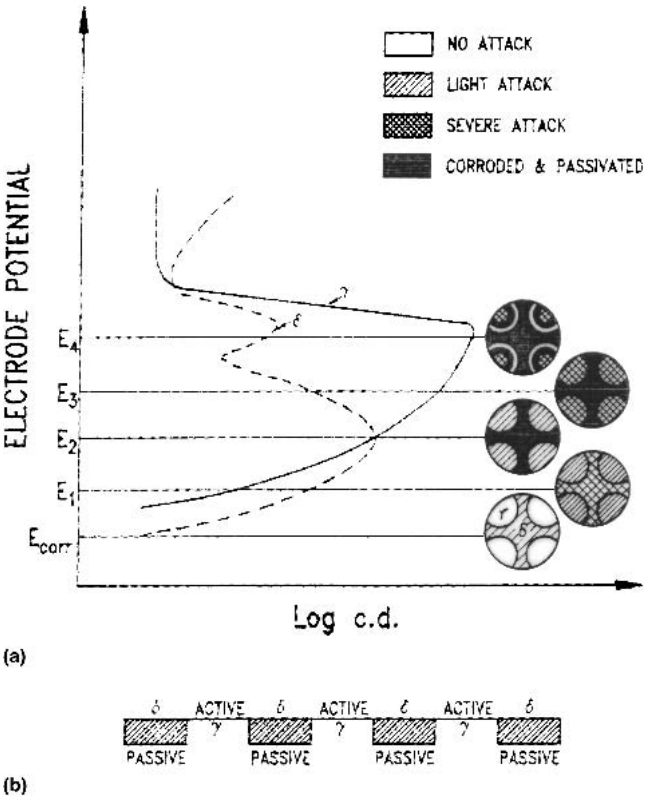

Fig. 11 (a) A model showing the active dissolution of the austenitic stainless steel weld metal; (b) active-passive sites formed on the weld metal surface during active dissolution

3.8 Model for Weld Metal Dissolution

To take into account the different microstructures observed after potentiostatic etching, and the role of ferrite in the weld metal corrosion, a model polarization diagram is proposed (Fig. 11a). In Fig. 11(a), schematic polarization diagrams of delta-ferrite and austenite are shown. Possible microstructural changes due to anodic polarization of a weld metal are dis-

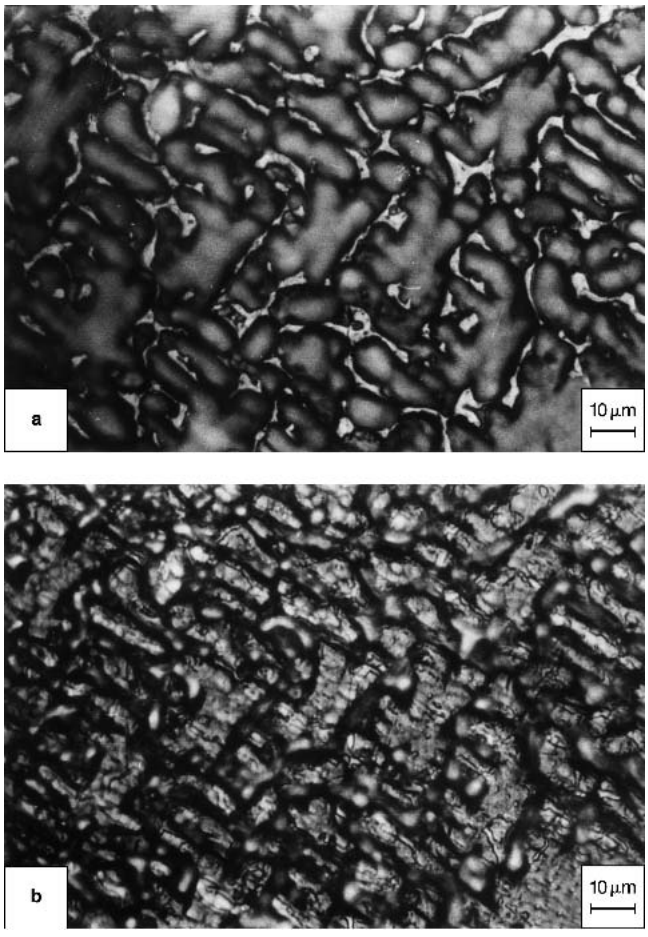

Fig. 12 Optical photomicrograph of specimen WA H2 (a) matrix-focused, showing the zones where dissolution has taken place and (b) matrix-defocused showing the finer structure inside the zones where the dissolution had taken place. The specimen was potentiostatically etched with deaerated 0.5 M H_2SO_4 + 0.1 g/L NH_4SCN at −250 mV (SCE).

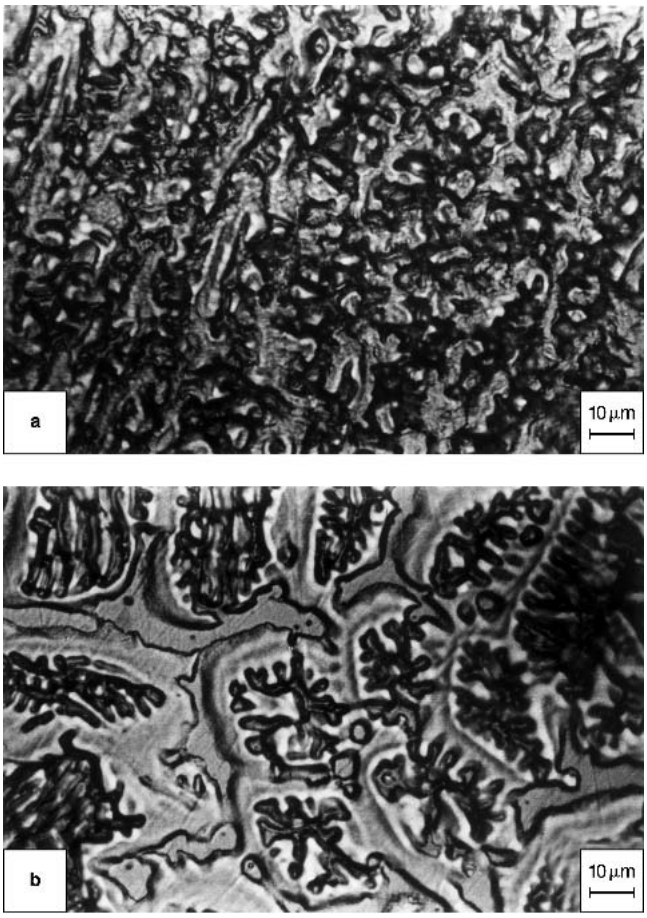

Fig. 13 (a) Photomicrograph of specimen WA H3 showing the corrosion attack on ferrite particles and its surrounding regions; and (b) photomicrograph of specimen Cr1H5 showing zones formed around ferrite, which was attacked. The specimen was potentiostatically etched with deaerated 0.5 M H_2SO_4 + 0.1 g/L NH_4SCN at −250 mV (SCE).

cussed as a function of the applied potential. At OCP, ferrite would be lightly attacked and austenite would remain cathodically protected. At the applied potential E_1, more of the ferrite undergoes corrosion attack, with a light attack on the austenite initiated. At E_2, increased attack (the maximum, as this is the primary passivation potential for ferrite) on ferrite and, correspondingly, more attack on austenite is expected, because austenite is the major component and is in its active dissolution region. At E_3, ferrite is already passivated and does not contribute to the dissolution current density, but austenite dissolution increases further. At E_4, austenite dissolves at its primary passivation potential, and ferrite is completely passivated.

To check the validity of this model, weld metal specimens were potentiostatically etched at –250 mV (SCE), which is very close to the E_{pp} for most of the specimens. Figure 12(a) is the photomicrograph of WA H2, showing islands where selective dissolution has taken place. To identify the substructure present in these islands, the matrix was defocused (Fig. 12b), wherein it was clearly observed that at the center of these islands the primary ferrite cores were attacked. This attack subsequently spread outward. As the dissolution increased with applied potential, the islands increased in size (area) and finally merged into each other. Figure 13(a) shows the clear attack on ferrite as well as on the surrounding region. Substantial attack on austenite was also noted as the etching was carried out close to the E_{pp}. The initial attack on ferrite, and the nearby regions rich in Cr, are attacked at very active potentials. These regions become partially passive after dissolution. Austenite around these passive regions with nominal Cr and Mo remain active (E_1 or E_2). The network of passive-active zones (Fig. 11b) throughout the surface accelerates the attack on the austenite matrix, and, thereby, the zonal area around ferrite increases. Subsequently, these regions merge into each other. Figure 13(b) shows the dissolution of ferrite and the surrounding austenite, forming a zonal area. It should also be noted from Fig. 13(b) that many zones are in close contact with each other. The austenite centers with the lowest amounts of Cr and Mo are the last ones to be attacked, as can be seen from Fig. 7(k).

As the ferrite and the Cr-rich regions around the ferrite dissolve, the enrichment of Mo takes place on the surface. A number of publications have reported the prominent role played by such an enrichment of Mo during active dissolution, which promoted the formation of Cr-oxyhydroxide film and inhibited further dissolution. In a way, the presence of Mo catalyzed the formation of such a passivating film emanating from ferrite and spreading outward into the austenite regions. Therefore, increased amounts of Mo in the weld metals showed a very drastic decrease in the critical anodic current density and E_{pp} values (Table 9).

4. Conclusions

Based on the microstructural and electrochemical studies carried out on the weld metal specimens with different heat inputs, the following conclusions were drawn.

- Potentiostatic etching can be effectively used to delineate various microconstituents such as ferrite, δ-γ interface boundaries, and interdendritic regions, which were depleted in Cr. These microstructural details could be further used to explain the weld metal corrosion characteristics.
- Electrochemical parameters were influenced by Mo more than Cr. Mo was found to be more effective in altering these parameters. The role of ferrite was found to be complementary to Cr and Mo, and acted independently to influence the electrochemical behavior of the weld metal.
- Most of the electrochemical parameters were unaffected by changes in the heat input. But there existed a correlation between the corrosion rate and the E_{pp}. It was found that as the E_{pp} became more active, corrosion rates drastically decreased. This correlation grew weaker, however, with the increase in heat input.
- A dissolution model for the austenitic weld metal was suggested that described the role of ferrite during dissolution. This validity of the model was confirmed with the help of potentiostatic etching experiments at –250 mV (SCE). According to this model, at particularly active potentials, the initial dissolution of the weld metal starts at the ferrite particles and then spreads laterally toward the austenite centers as the potential becomes slowly nobler.

Acknowledgments

The authors wish to thank Dr. V.S. Raghunathan, Associate Director, Materials Characterisation Group (MCG), for his keen interest and support during the course of this investiga-

Table 9 Primary passivation potential and peak current density values of the weld metals

Heat input	WA		Cr1		Cr2		Mo1		Mo2	
	E_{pp}, mV	CD, μA/cm²	E_{pp}, mV	CD, μA/cm²	E_{pp}, mV	CD, μA/cm²	E_{pp}, mV	CD, μA/cm²	E_{pp}, mV	CD, μA/cm²
H1	−194	6506	−199	4567	−218	4506	−201	3598	−218	629
H2	−195	6893	−195	5321	−213	4274	−197	4115	−217	750
H3	−189	6075	−198	4688	−219	4900	−200	3747	−224	596
H4	−188	7124	−197	7127	−219	4993	−210	4267	−218	478
H5	−185	7257	−187	4438	−211	5108	−195	3029	−207	1371

tion. The assistance of Smt. K. Parimala for specimen preparation is gratefully acknowledged.

References

1. F.C. Brautigam, Welding Practices That Minimize Corrosion. Pt. 2, *Chem. Eng.,* Vol 84, 1977, pp 97-98, 100, 102
2. M.A. Streicher, "Theory and Application of Evaluation Tests for Detecting Susceptibility to Intergranular Attack in Stainless Steels and Related Alloys: Problems and Opportunities," STP 656, *Annual Book of ASTM Standards,* ASTM, 1978, p 70
3. A. Garner, The Effect of Autogenous (TIG) Welding on Chloride Pitting Corrosion in Austenitic Stainless Steels, *Corrosion,* Vol 35, 1979, p 108-114
4. O. Hammar and U. Svenson, Influence of Steel Composition on Segregation and Microstructure During Solidification of Austenitic Stainless Steels, *Solidification and Casting of Metals,* The Metals Society, London, 1979, p 401
5. R.A. Farrar, Influence of Microsegregation on Phase Transformations and Properties of Type 316 Weld Metals at Elevated Temperatures, *Stainless Steels '84,* The Institute of Metals, London, 1986, p 336-342
6. M. Lindenmo, Microstructural Factors Affecting Pitting Resistance of Weld Metal of Highly Alloyed Austenitic Stainless Steels, *Stainless Steels '84,* The Institute of Metals, London, 1986, p 262-270
7. M.J. Cieslak and W.F. Savage, Ferrite Morphology in High Molybdenum Stainless Steels (Technical Note), *Welding J.,* Vol 60, 1981, p 131s-134s
8. T.G. Davey, T.G. Gooch, and J.L. Robinson, An Assessment of Flux-Cored Wire Welding Type 316L Austenitic Stainless Steel: Part 1, *Metal Construct.,* Vol 19, 1987, p 431-433, 435
9. F.C. Hull, Effect of Delta-Ferrite on the Hot Cracking of Stainless Steel, *Welding J.,* Vol 46, 1967, p 399s-409s
10. A. Garner, How Stainless Steel Welds Corrode, *Metal Prog.,* Vol 127, 1985, p 31-32, 34-36
11. K.F. Krysiak, Cause and Prevention of Unusual Failures of Materials, *Corrosion/83,* National Association of Corrosion Engineers, 1983, p 16
12. M. Henthorne, Corrosion Testing of Weldments, *Corrosion,* Vol 30, 1974, p 39-46
13. P.I. Marshall and T.G. Gooch, Effect of Composition on Corrosion Resistance of High Alloy Austenitic Stainless Steel Weld Metals, *Corrosion,* Vol 49, 1993, p 514-526
14. U.K. Mudali, R.K. Dayal, T.P.S. Gill, and J.B. Gnanamoorthy, Influence of Nitrogen Addition on Microstructure and Pitting Corrosion Resistance of Austenitic Weld Metals, *Werk. Korrosion,* Vol 37, 1986, p 637-643
15. M.G. Pujar, U.K. Mudali, R.K. Dayal, and T.P.S. Gill, Susceptibility of As-Welded and Thermally Aged Type 316LN Weldments Toward Pitting and Intergranular Corrosion, *Corrosion,* Vol 48, 1992, p 579-586
16. Gas Tungsten Arc Welding, *Welding Handbook,* 8th ed., Vol 2, R.L. O'Brien, Ed., American Welding Society, 1991, Chap. 3, p 82
17. "Standard Procedure for Calibrating Magnetic Instruments to Measure the Delta-Ferrite Content of Austenitic Stainless Steel Weld Metal," AWS A4.2-74, American Welding Society, 1974
18. "Standard Reference Test Method for Making Potentiostatic and Potentiodynamic Anodic Polarization Measurements," ASTM-G:5-94, *Annual Book of ASTM Standards,* ASTM, 1995, p 48-58
19. T.G. Gooch, Corrosion of AISI Type 304 Austenitic Stainless Steel, *Br. Welding J.,* Vol 15, 1968, p 345-357
20. "Standard Test Method for Conducting Potentiodynamic Polarization Resistance Measurements," ASTM-G:59-91, *Annual Book of ASTM Standards,* 1995, p 216-219
21. S. Barnartt, Two-Point and Three-Point Methods for the Investigation of Electrode Reaction Mechanism, *Electrochem. Acta,* Vol 15, 1970, p 1313-1324
22. M.J. Danielson, An Evaluation of the Three-Point Method to Measure Corrosion Rates, *Corrosion,* Vol 38, 1982, p 580-586
23. C.D. Lundin, T.P.S. Gill, C.Y.P. Qiao, Y. Wang, and K.K. Khan, Weldability of Low-Carbon Micro-alloyed Steels for Marine Structures, *WRC Bull.,* Vol 359, 1990, p 15
24. N. Suutala, Effect of Solidification Conditions on the Solidification Mode in Austenitic Stainless Steel Welds, *Met. Trans. A,* Vol 14A, 1983, p 191-197
25. W.T. DeLong, Ferrite in Austenitic Stainless Steel Weld Metal, *Welding J.,* Vol 53, 1974, p 273s-286s
26. D.J. Kotecki and T.A. Siewert, WRC-1992 Constitution Diagram for Stainless Steel Weld Metals: *a* Modification of the WRC-1988 Diagram, *Welding J.,* Vol 71, 1992, p 171s-178s
27. S.A. David, Ferrite Morphology and Variations in Ferrite Content in Austenitic Stainless Steel Welds, *Welding J.,* Vol 60, 1981, p 63s-71s
28. J.A. Brooks and A.W. Thompson, Microstructural Development and Solidification Cracking Susceptibility of Austenitic Stainless Steel Welds, *Int. Mater. Rev.,* Vol 36, 1991, p 16-44
29. J.A. Brooks, J.C. Williams, and A.W. Thompson, Solidification and Solid State Transformations of Austenitic Stainless Steel Welds, *Trends in Welding Research,* S.A. David, Ed., American Society for Metals, 1982, p 331-357
30. J.A. Brooks, A.W. Thompson, and J.C. Williams, A Fundamental Study of the Beneficial Effects of Delta Ferrite in Reducing Weld Cracking, *Welding J.,* Vol 63, 1983, p 71s-83s
31. M.A.A. Tullmin and F.P.A. Robinson, Effect of Molybdenum Additions on the Corrosion Resistance of a 12% Chromium Steel, *Corrosion,* Vol 44, 1988, p 664-670
32. E.A. Lizlovs, Effects of Mo, Cu, Si and P on Anodic Behaviour of 17Cr Steels, *Corrosion,* Vol 22, 1966, p 297-308
33. M.B. Rockel, Effect of Mo on the Corrosion Behavior of Fe-Cr Alloys, *Corrosion,* Vol 29, 1973, p 393-396
34. Corrosion In Aqueous Solution, *Metal/Environment Reaction,* Vol 1, 3rd ed., L.L. Shreir, R.A. Jarman, and G.T. Burstein, Ed., Butterworth-Heinemann, Oxford, 1994, p 52-113
35. N.D. Greene, Predicting Behavior of Corrosion Resistant Alloys by Potentiostatic Polarization Methods, *Corrosion,* Vol 18, 1962, p 136t
36. A.P. Bond and E.A. Lizlovs, Anodic Polarisation of Austenitic Stainless Steels in Chloride Media, *J. Electrochem. Soc.,* Vol 15, 1968, p 1130-1135
37. Y.H. Yau and M.A. Streicher, The Effect of Chromium Content (0-35%) in Fe–Cr Alloys on Corrosion Rates and Mechanisms in 1.0N Sulfuric Acid, *Corrosion,* Vol 47, 1991, p 352-359
38. C.-O.A. Olsson, The Influence of Nitrogen and Molybdenum on Passive Films Formed on the Austeno-Ferritic Stainless Steel 2205 Studied by AES and XPS, *Corrosion Sci.,* Vol 37, 1995, p 467-479
39. K. Asami, M. Naka, K. Hashimoto, and T. Masumoto, Effect of Molybdenum on the Anodic Behavior of Amorphous Fe–Cr–Mo–B Alloys in Hydrochloric Acid, *J. Electrochem. Soc.,* Vol 127, 1980, p 2130-2138
40. K. Sugimoto and Y. Sawada, Role of Mo Additions to Austenitic Stainless Steels in the Inhibition of Pitting in Acid Chloride Solutions, *Corrosion Sci.,* Vol 17, 1977, p 425-445
41. J.W. Johnson, M.S. Lee, and W.J. James, Electrochemical Behaviour of Molybdenum in Acid Chloride Solutions, *Corrosion,* Vol 26, 1970, p 507-510
42. P.Y. Park, E. Akiyama, A. Kawashima, K. Asami, and K. Hashimoto, The Corrosion Behavior of Sputter-Deposited Cr-Mo Alloys in 12 M HCl Solution, *Corrosion Sci.,* Vol 37, 1995, p 1843-1860